

Electronic Supplementary Information
for
Confinement-enhanced Li⁺ ion dynamics in an ionic liquid-based electrolyte in
porous materials

By Janis Hessling,^a Martin Lange^b and Monika Schönhoff*^a

^a Institute of Physical Chemistry, University of Münster, Corrensstraße 28/30, D-48149 Münster, Germany

^b Institute of Inorganic and Analytical Chemistry, University of Münster, Corrensstraße 28/30, D-48149
Münster, Germany

A. Phase behavior and calculation of filling degree

A detection of the melting transition of ionic liquid, which disappears upon immobilization in micropores, serves to determine the amount of liquid electrolyte required for pore saturation. The DSC measurements were performed using a Netzsch DSC 204 differential scanning calorimeter. The samples were prepared in an argon filled glove box and hermetically sealed in aluminum pans. They were first cooled to 193 K and then heated to 423 K, with a fixed scan rate of 5 K min⁻¹. This cooling and heating cycle was repeated two times. The DSC heating traces recorded during the second heating step are shown in Fig. S1 (a-c).

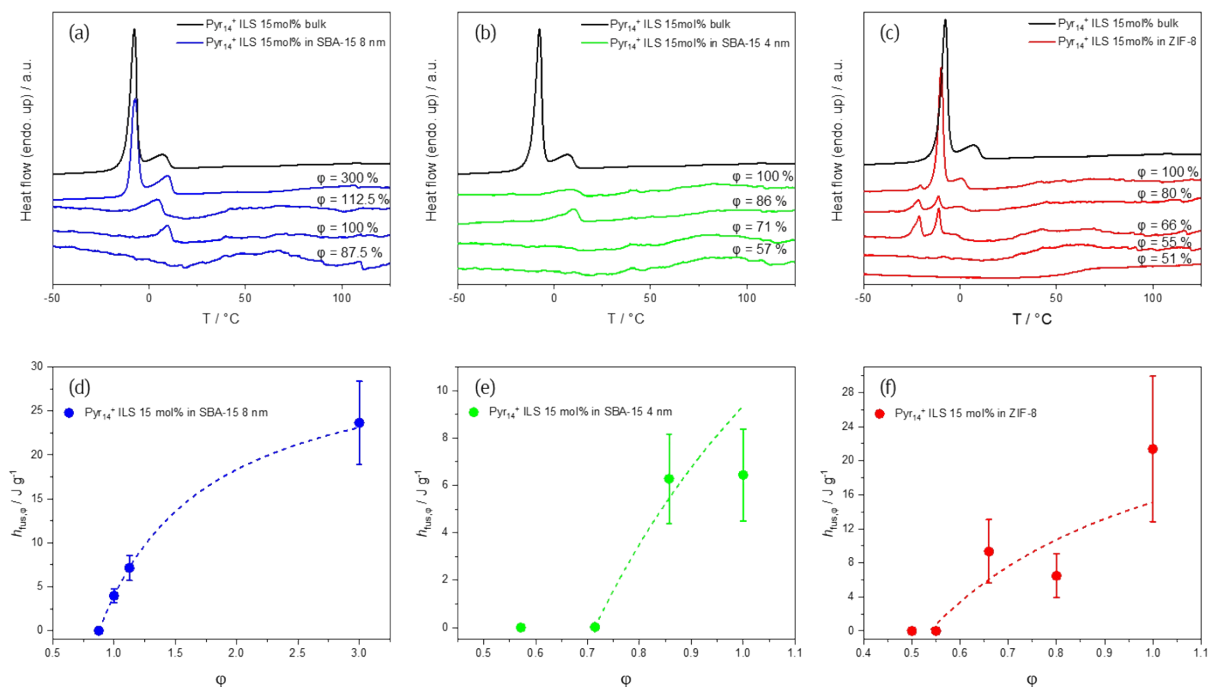


Figure S1. DSC heating traces of Pyr₁₄TFSA-LiTFSA at a Li salt concentration of 15 mol% mixed with the porous materials SBA-15 8 nm (a), SBA-15 4 nm (b) and ZIF-8 (c) at different nominal filling degree φ . Enthalpy of fusion $h_{fus,\varphi}$ of Pyr₁₄TFSA-LiTFSA at a Li salt concentration of 15 mol% mixed with the porous materials SBA-15 8 nm (d), SBA-15 4 nm (e) and ZIF-8 (f) in dependence on the theoretical filling degree φ with a fit of eq S4.

The nominal filling degree φ was calculated using eq. S1.

$$\varphi = \frac{V_{ILS}}{V_p} = \frac{m_{ILS} \cdot m_p \cdot v_p}{\rho_{ILS}} \quad (S1)$$

Here, V_{ILS} is the volume of the electrolyte, V_p the pore volume, m_{IL} and m_p the weighted masses of the electrolyte and the porous materials, ρ_{ILS} the density of the electrolyte (1.40 g cm⁻³) and v_p the specific pore volume of the porous materials as given by literature or the manufacturer (ZIF-8 ^{S1}: 0.636 cm³ g⁻¹ / SBA-15 8 nm ^{S2}: 0.8 – 1.0 cm³ g⁻¹, calculated with 0.8 cm³ g⁻¹ / SBA-15 4 nm ^{S3}: 0.7 – 0.9 cm³ g⁻¹, calculated with 0.7 cm³ g⁻¹)

The fit is based on the assumption that there are two species of electrolyte in the mixture of the electrolyte and the porous materials. On the one hand a confined species which does not have a specific enthalpy of fusion and on the other hand a free species which has the specific enthalpy of fusion of the bulk electrolyte $h_{fus,0}$. It follows that the enthalpy of fusion of the mixture of electrolyte and porous material h_{fus} can be described by eq. S2.

$$h_{fus} = h_{fus,0} \cdot z \quad (S2)$$

Here, z is the fraction of free electrolyte, which is given by the maximum filling degree φ_{max} and the nominal filling degree φ according to

$$z = \frac{\varphi - \varphi_{max}}{\varphi} \quad (S3)$$

By inserting eq. S3 in eq. S2 we get eq. S4.

$$h_{fus} = h_{fus,0} \cdot \left(1 - \frac{\varphi_{max}}{\varphi}\right) \quad (S4)$$

Since $h_{fus,0}$ is the specific enthalpy of fusion of the bulk electrolyte, it has a fixed value (measured as 32.69 J/g) and therefore φ_{max} is the only variable in eq S4. Furthermore, eq S4 is only valid for $\varphi_{max} < \varphi$, because for $\varphi_{max} \geq \varphi$ no enthalpy of fusion is measurable.

The values of φ_{max} for the different porous materials are listed in Table S1.

Table S1. φ_{max} for SBA-15 8 nm, SBA-15 4 nm and ZIF-8

porous material	SBA-15 8 nm	SBA-15 4 nm	ZIF-8
φ_{max}	88%	71%	54%

With this maximum filling degree and the number of cages per mol of ZIF-8 (1.0·10²³ cages/mol)^{S4, 5}, the number of ion pairs per cage was calculated to be approximately 2 on average. The values of φ_{max} show that saturation of the porous materials with IL occurs well below the nominal volume. There are two approaches to an explanation. On the one hand the micropore volumes of the porous materials are on the order of magnitude of the van der Waals volumes of ions of the electrolyte. For example, the TFSA⁻ anion has a van der Waals volume of 147 Å³ ^{S6} and ZIF-8 a micropore volume of 817 Å³.^{S1} Thus, sterical reasons may well prohibit a complete filling of the micropore volume. Sterical problems would have a more severe effect for smaller pore sizes, which could explain the lowest φ_{max} for ZIF-8 and correspondingly larger values for the SBA materials. On the other hand the particle sizes of the used porous materials are quite large (SBA-15: 150 μm, ZIF-8: 5 μm). Here, the center of the particles might be out of reach for the electrolyte, resulting in a lower φ_{max} than expected.

The values of φ_{\max} from Table S1 were used to prepare both, confined IL and ILS, assuming that the saturation point of Li salt-containing liquids is the same as that of pure IL.

B. FTIR spectra

The FTIR spectra were recorded using a FTIR spectrometer IFS 66v/s, (Bruker), equipped with a MCT detector. KBr pellets were prepared in a glove box under Ar atmosphere by mixing the samples with KBr and homogenizing them using a mortar and pestle. The mixtures, which had a total mass of 300 mg with approximately 2 wt% of sample were pressed outside of the glove box with 0.7 GPa to pellets with a diameter of 13 mm. Prior to measurement the pellets were heated for 1 h at 100 °C and 10^{-6} bar to eliminate any water potentially absorbed during the pressing process.

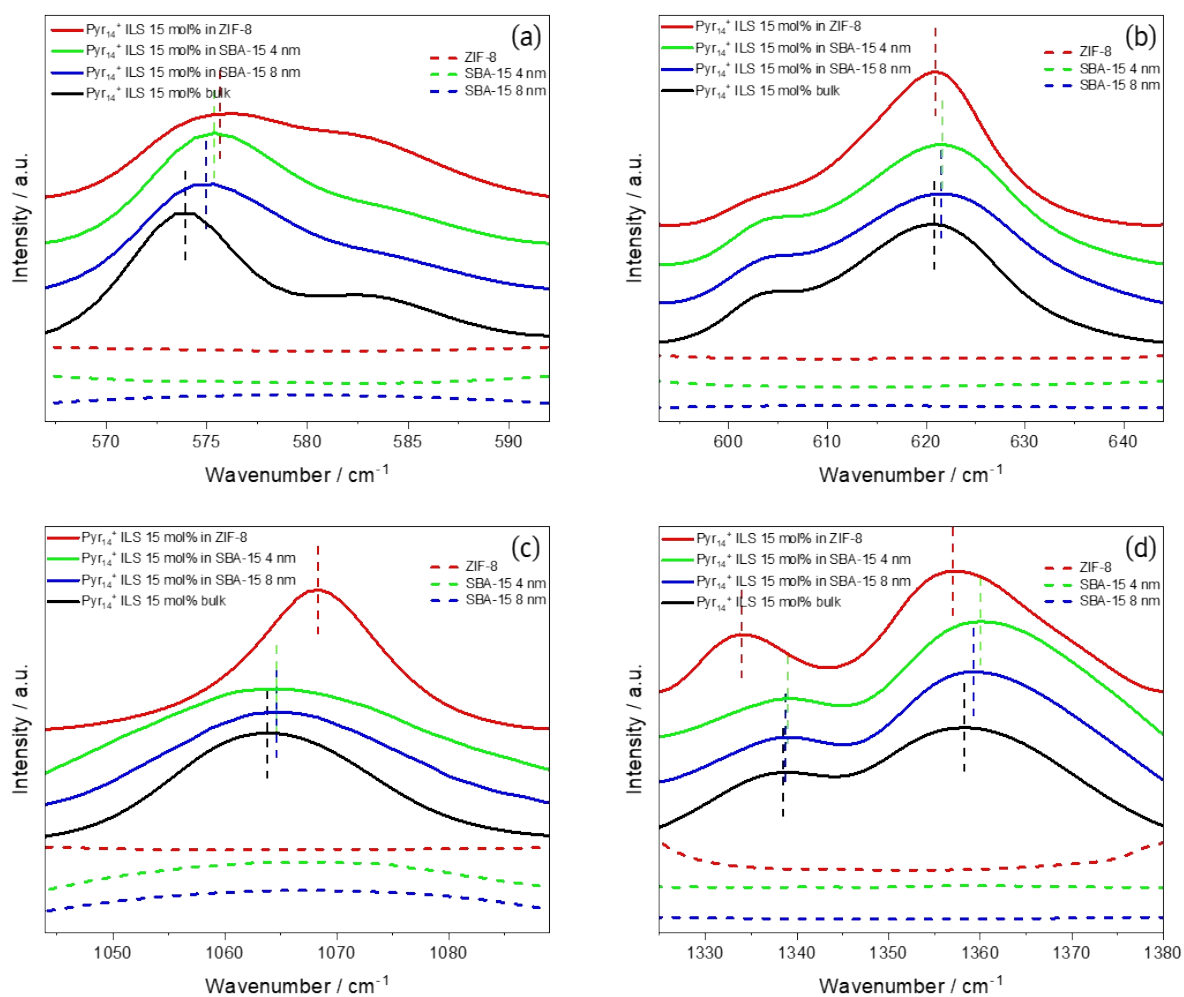


Figure S2. IR spectra of CF_3 asymmetric bending (a), SO_2 asymmetric bending (b), SNS asymmetric stretching (c) and SO_2 asymmetric stretching (d) of the TFSA-anion of $\text{Pyr}_{14}\text{TFSA}_{(1-x)}\text{LiTFSA}_x$ in bulk, confined in ZIF-8 and confined in SBA-15 at a Li salt concentration of 15 mol%.

C. XRPD patterns

X-ray diffraction measurements were recorded with a STOE StadiP diffractometer in Debye-Scherrer geometry with a Dectris MYTHEN2 1K detector to evaluate the phase purity of the synthesized compounds. The radiation source was $Cu K_{\alpha}$ ($\lambda = 1.5406 \text{ \AA}$) employing a Ge(111) monochromator. The diffraction data was collected within a 2θ -range of 5 to 70 degree, with a step size of 0.015 2θ in PSD moving scan mode with a step width of 3 2θ and 240 seconds per step. For each composition, three consecutive measurements were performed and the results were summed to obtain the final diffractogram. All samples were measured in sealed borosilicate glass capillaries (Hilgenberg, outer diameter of 0.5 mm), which were prepared in the glove box. To confirm phase purity, Pawley fitting via Topas was applied to XRPD patterns of all samples, proving the accordance to reference literature. The results, together with respective reference values, are given in Table S2.

Table S2. Fit results for PXRD Pawley Fits of Zif-8 and ZIF-8 with confined $Pyr_{14}TFSA_{(1-x)}LiTFSA_x$.

	Zif-8 pure	Zif-8 Pyr14
Ref. database no	COD 4118891	CCDC 1058659
Space group	I-43m	I-43m
Rwp	6.21	3.63
GOF	2.91	1.52
a = b = c	17.023(1)	17.084(1)
al = be = ga	90	90

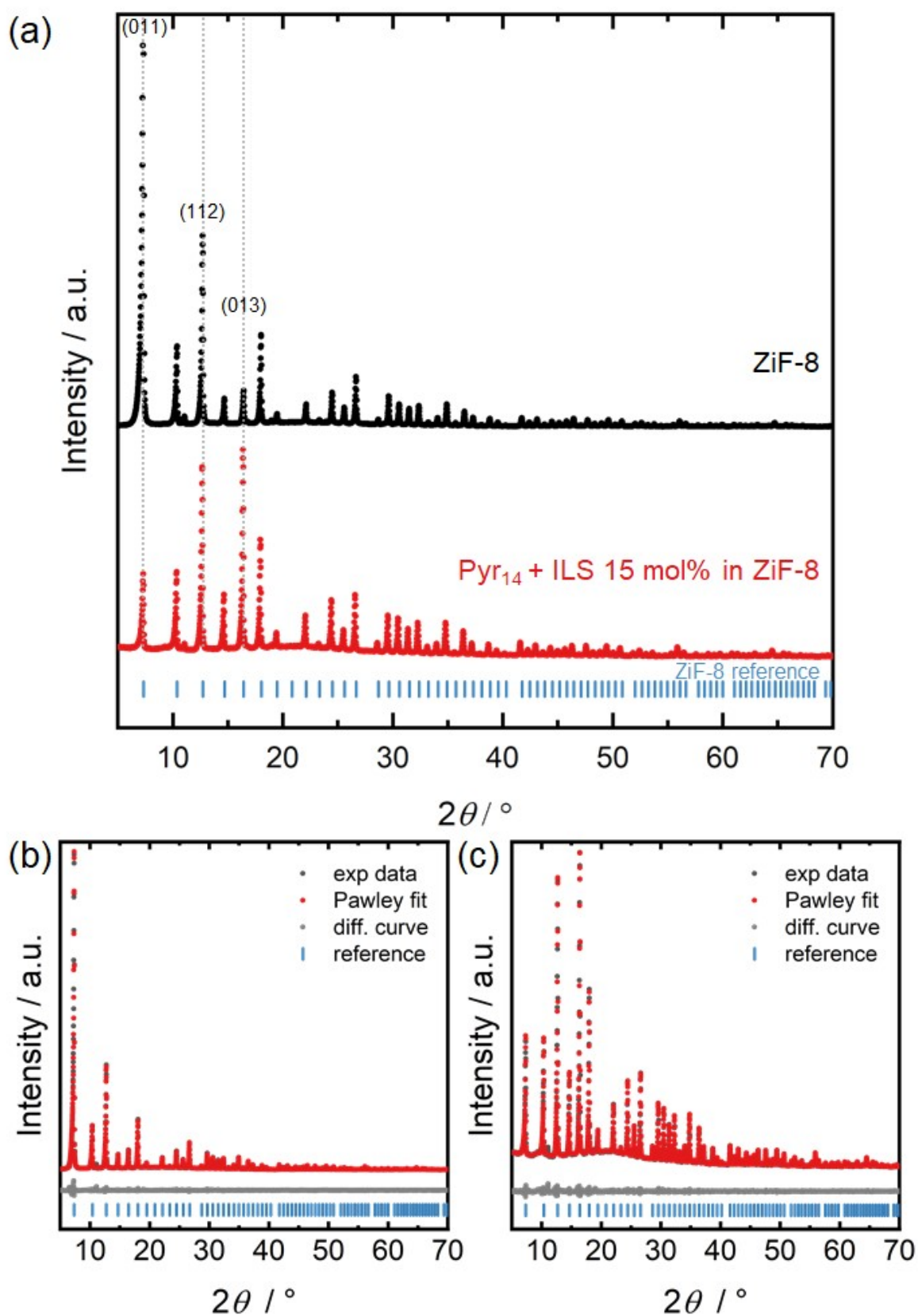


Figure S3. (a) XRPD patterns of ZIF-8 (black) and ZIF-8 with confined Pyr₁₄TFSA_(1-x)LiTFSA_x (red) at a Li salt concentration of 15 mol%. Plane indices were assigned with reference to a previous study, showing the reported change of relative intensity values with solvent inclusion.¹ (b) Pawley fit results for ZIF-8 and (c) for Pyr₁₄TFSA_(1-x)LiTFSA_x. Respective fitting values are given in Table S2.

D. Raman spectra

$\nu(\text{Zn-N})$ mode of ZIF-8

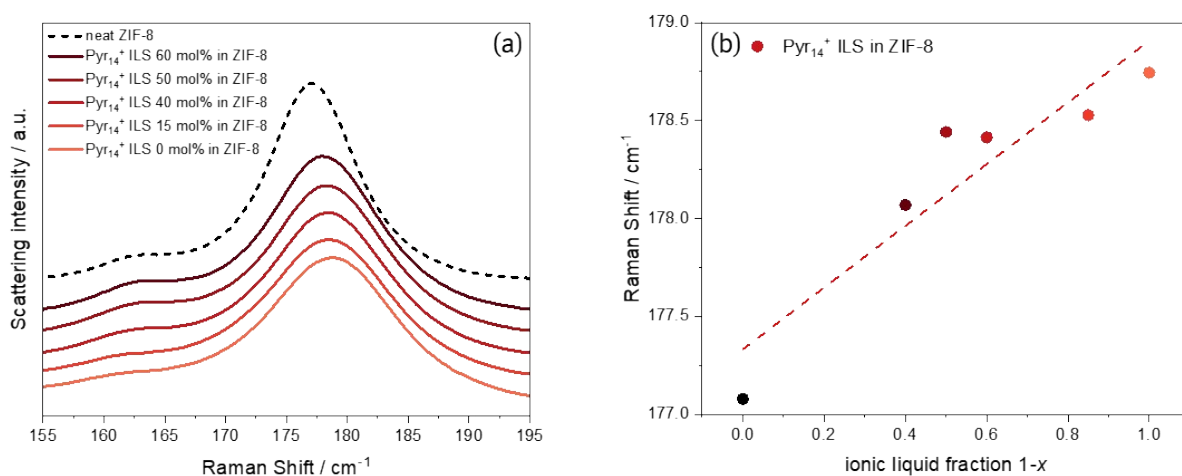


Figure S4. (a) Raman spectra of the $\nu(\text{Zn-N})$ mode of neat ZIF-8 and ZIF-8 with confined $\text{Pyr}_{14}^+\text{TFSA}_{(1-x)}\text{LiTFSA}_x$ at different Li salt fractions, in the spectral region between 155 and 195 cm^{-1} . (b) Raman Shift of the $\nu(\text{Zn-N})$ mode of the ZIF-8 framework in dependence on the ionic liquid fraction.

Pyr_{14}^+ isomers

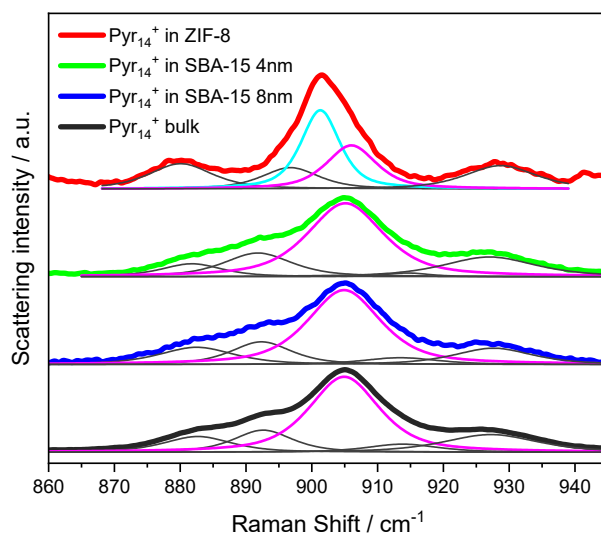


Figure S5. Raman spectra of the Pyr_{14}^+ isomers of $\text{Pyr}_{14}^+\text{TFSA}_{(1-x)}\text{LiTFSA}_x$ in bulk, confined in ZIF-8 and confined in SBA-15 at a Li salt fraction of 15 mol%, in the spectral region between 860 and 945 cm^{-1} , with spectral deconvolution according to literature.⁷ Contributions include the characteristic Raman band of the Pyr_{14}^+ isomer with the butyl-chain in equatorial position (magenta) and in axial position (cyan).

TFSA⁻-anions

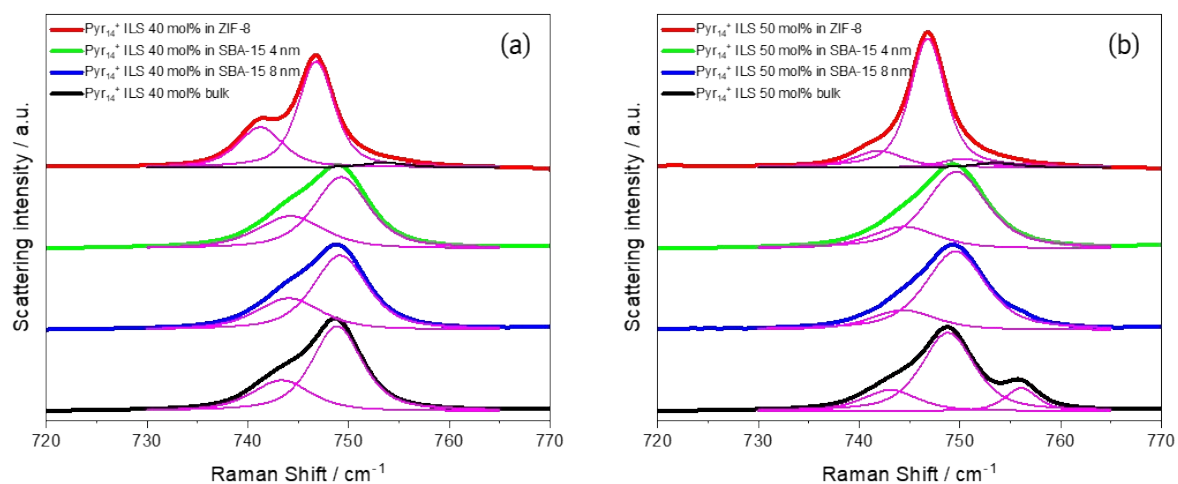


Figure S6. Raman spectra of Pyr₁₄TFSA_(1-x)LiTFSA_x in bulk, confined in ZIF-8 and confined in SBA-15, in the spectral region between 720 and 770 cm⁻¹ for the Li fractions x = 0.40 (a) and x = 0.50 (b). Purple lines are obtained by deconvolution using Voigt profiles.

E. Temperature dependent ⁷Li spin-lattice relaxation rates

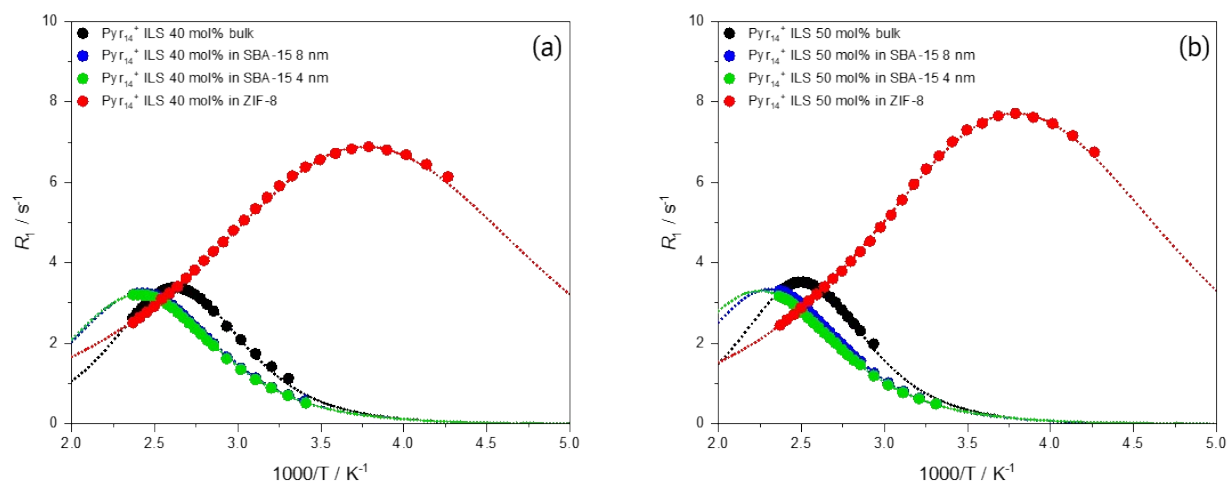


Figure S7. Temperature dependent ⁷Li spin-lattice relaxation rates of Pyr₁₄TFSA_(1-x)LiTFSA_x in bulk, confined in ZIF-8 and confined in SBA-15 for the Li fractions x = 0.40 (a) and x = 0.50 (b). Dotted lines are fits obtained from the BPP-model.

F. Fitting of data sets with the BPP model

To fit the temperature dependent spin-lattice relaxation rate R_1 the Bloembergen, Purcell and Pound (BPP) model^{S8} can be applied. With the assumption of one random isotropic motional mode with one correlation time τ_c R_1 can be described in the case for quadrupole interactions by eq. S5.

$$R_1 = \frac{1}{T_1} = A_{quad} \cdot \left(\frac{\tau_c}{1 + \omega_0^2 \tau_c^2} + \frac{4\tau_c}{1 + 4\omega_0^2 \tau_c^2} \right) \quad (S5)$$

For $R_{1,max}$ eq. S6 is valid.

$$\omega_0 \tau_{c,max} = 0.616 \quad (S6)$$

With $R_{1,max}$ and $\tau_{c,max}$, A_{quad} can be derived from eq. S5. To obtain the correlation time at a given relaxation rate, eq. S5 can be transformed to a polynomial equation of fourth order in τ_c .

$$4 \frac{R_1}{A_{quad}} \omega_0^4 \tau_c^4 - 8 \omega_0^2 \tau_c^3 + 5 \frac{R_1}{A_{quad}} \omega_0^2 \tau_c^2 - 5 \tau_c + \frac{R_1}{A_{quad}} = 0 \quad (S7)$$

Solving eq. S7, the correlation time for each relaxation rate measured at a certain temperature can be obtained. The correlation times then can be plotted against the temperature, as shown in Figure S8. If the BPP-model is valid, the temperature dependence can be described with Arrhenius behaviour.

$$\tau_c = \tau_0 \cdot \exp\left(\frac{E_a}{RT}\right) \quad (S8)$$

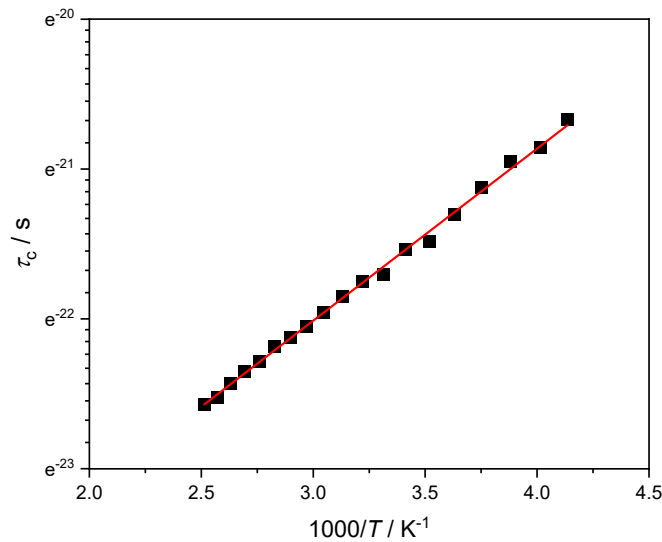


Figure S8. Temperature dependent ${}^7\text{Li}$ correlation times of $\text{Pyr}_{14}\text{TFSA}_{(1-x)}\text{LiTFSA}_x$ confined in ZIF-8 for the Li fraction $x = 0.15$. The red line is the Arrhenius fit with eq. (S8)

Fitting of data sets without $R_{1,max}$

The value of $R_{1,max}$ is crucial for the fitting with the BPP model. When $R_{1,max}$ is not available experimentally one has to make reasonable assumptions about the values of $R_{1,max}$. Following a procedure of Hammer *et al.*^{S9} we make those assumptions to obtain limiting values for A_{quad} according to eq. S5 and S6.

With the value of χ^2 the quality of an obtained fit can be described. It is given by:

$$\chi^2 = \sum_{i=1}^N \left(\frac{y_i - y(x_i; a_1 \dots a_M)}{\sigma_i} \right)^2 \quad (S9)$$

For a good fit the value of χ^2 is small. A fit of moderate quality is achieved when χ^2 is around the number of degrees of freedom F , which is the number of experimental data points N subtracted by the number of fitting parameters M .¹⁰ In our case $N = 21$ and $M = 2$. Therefore, a fit of moderate quality is achieved when χ^2 is around 19.

In our procedure, fits of $R_1(T)$ data were performed, assuming a range of different values of $R_{1,max}$, and calculating the value of χ^2 . We limited the assumed values of $R_{1,max}$ to those that allow a fit of moderate quality, i.e. χ^2 remaining smaller than 19. This yields upper and lower limits for $R_{1,max}$ with a still moderate fit quality. The resulting fits for the accepted limits of $R_{1,max}$ (upper and lower limit) are shown in Figure S9. In Table S3 and Figure S10 the values for optimized fits as well as the fits for the upper and lower limits are summarized. The optimum value of $R_{1,max}$ was chosen such that χ^2 is minimal. The differences of the parameters derived from the respective *max*, *min* and *opt* fits are not very large, proving that the fitting is reasonable even without $R_{1,max}$ directly derived from experiment. Only in one case (upper limit for A_{quad} and τ_c of Pyr₁₄TFSA_(1-x)LiTFSA_x confined in SBA-15 8 nm for $x = 0.6$) the upper limits are too high to allow further interpretation.

Table S3. Fit results from BPP analysis of Pyr₁₄TFSA_(1-x)LiTFSA_x confined in SBA-15 8 nm and SBA-15 4 nm for the Li salt fractions $x = 0.5$ and $x = 0.6$. Max, min: Corresponding to fits with upper and lower limit of $R_{1,max}$, and yielding $\chi^2 = 19$.

sample	fit	$A_{quad} / (10^9 \cdot s^{-1})$	$\tau_0 / (10^{-12} s)$	$E_A / (kJ \cdot mol^{-1})$	χ^2
Pyr ₁₄ ⁺ ILS 50 mol% in SBA-15 8 nm	max	2.42	2.13	21.2	19.00
	opt	2.32	1.34	22.4	4.35
	min	2.28	0.97	23.3	19.00
Pyr ₁₄ ⁺ ILS 60 mol% in SBA-15 8 nm	max	3.49	4.90	21.0	19.00
	opt	2.62	2.16	22.5	3.21
	min	2.35	1.27	23.7	19.00
Pyr ₁₄ ⁺ ILS 50 mol% in SBA-15 4 nm	max	2.51	3.99	19.7	19.00
	opt	2.28	1.98	21.4	2.82
	min	2.20	1.24	22.6	19.00
Pyr ₁₄ ⁺ ILS 60 mol% in SBA-15 4 nm	max	11.9	36.8	18.8	19.00
	opt	2.80	4.25	20.8	3.41
	min	2.30	2.07	22.3	19.00

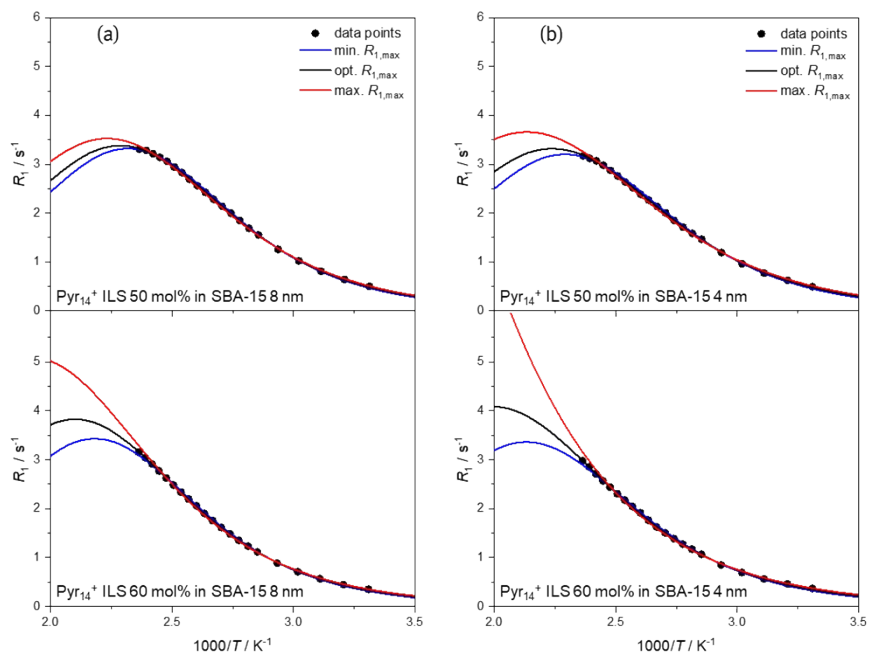


Figure S9. Temperature dependent ^7Li spin-lattice relaxation rates of $\text{Pyr}_{14}\text{TFSA}_{(1-x)}\text{LiTFSA}_x$ for the Li salt fractions $x = 0.50$ and $x = 0.60$ confined in SBA-15 8 nm (a) and SBA-15 4 nm (b). Fit curves from BPP analysis for max. A_{quad} (red line), opt. A_{quad} (black line) and min. A_{quad} (blue line).

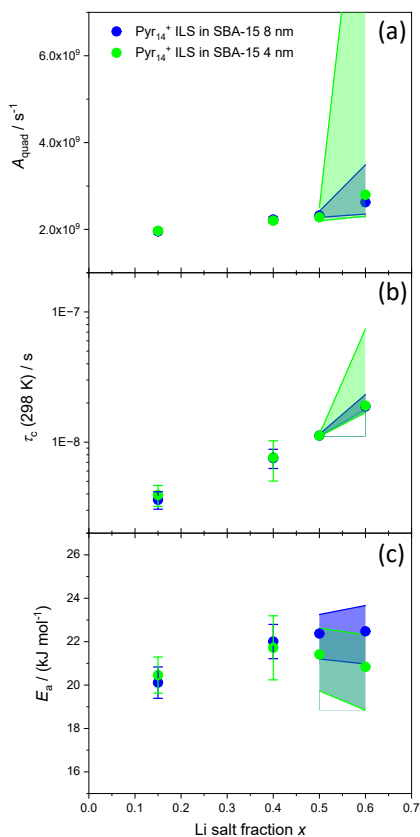


Figure S10. BPP fit parameters prefactor A_{quad} (a), correlation time τ_c at 298 K (b) and activation energy E_a (c) of $\text{Pyr}_{14}\text{TFSA}_{(1-x)}\text{LiTFSA}_x$ confined in SBA-15 8 nm and SBA-15 4 nm resulting from the free fit (blue and green circles and error bars) and the fit with fixed high and low prefactors A_{quad} (blue and green areas indicate maximum and minimum values).

Literatur

- S1. Park, K. S.; Ni, Z.; Côté, A. P.; Choi, J. Y.; Huang, R.; Uribe-Romo, F. J.; Chae, H. K.; O'Keeffe, M.; Yaghi, O. M., Exceptional chemical and thermal stability of zeolitic imidazolate frameworks. *Proc. Natl. Acad. Sci. U.S.A.* **2006**, *103* (27), 10186-10191.
- S2. SIGMA-ALDRICH, technical data sheet SBA-15 pore size 8 nm. https://www.sigmaaldrich.com/specification-sheets/186/067/806854-BULK_ALDRICH.pdf.
- S3. SIGMA-ALDRICH, technical data sheet SBA-15 pore size 4 nm. https://www.sigmaaldrich.com/specification-sheets/352/281/806803-BULK_ALDRICH.pdf.
- S4. Nozari, V.; Calahoo, C.; Tuffnell, J. M.; Adelhalm, P.; Wondraczek, K.; Dutton, S. E.; Bennett, T. D.; Wondraczek, L., Sodium Ion Conductivity in Superionic IL-Impregnated Metal-Organic Frameworks: Enhancing Stability Through Structural Disorder. *Sci. Rep.* **2020**, *10* (1), 3532.
- S5. Ban, Y.; Li, Z.; Li, Y.; Peng, Y.; Jin, H.; Jiao, W.; Guo, A.; Wang, P.; Yang, Q.; Zhong, C.; Yang, W., Confinement of Ionic Liquids in Nanocages: Tailoring the Molecular Sieving Properties of ZIF-8 for Membrane-Based CO₂ Capture. *Angew. Chem., Int. Ed.* **2015**, *54* (51), 15483-7.
- S6. Ue, M.; Murakami, A.; Nakamura, S., A Convenient Method to Estimate Ion Size for Electrolyte Materials Design. *J. Electrochem. Soc.* **2002**, *149* (10), A1385-A1388.
- S7. Umebayashi, Y.; Mitsugi, T.; Fujii, K.; Seki, S.; Chiba, K.; Yamamoto, H.; Lopes, J. N. C.; Pádua, A. A. H.; Takeuchi, M.; Takeuchi, M., Raman Spectroscopic Study, DFT Calculations and MD Simulations on the Conformational Isomerism of N-Alkyl-N-methylpyrrolidinium Bis-(trifluoromethanesulfonyl) Amide Ionic Liquids. *J. Phys. Chem. B* **2009**, *113* (13), 4338-4346.
- S8. Bloembergen, N.; Purcell, E. M.; Pound, R. V., Relaxation Effects in Nuclear Magnetic Resonance Absorption. *Physical Review* **1948**, *73* (7), 679-712.
- S9. Hammer, R.; Schönhoff, M.; Hansen, M. R., Comprehensive Picture of Water Dynamics in Nafion Membranes at Different Levels of Hydration. *J. Phys. Chem. B* **2019**, *123* (39), 8313-8324.
- S10. Press, W. H.; Teukolsky, S. A.; Vetterling, W. T.; Flannery, B. P., *Numerical Recipes in C*. Cambridge University Press: 1992.